Nano Research 2018, 11(4): 2149–2158
https://doi.org/10.1007/s12274-017-1832-8
Research Article
ISSN 1998-0124
CN 11-5974/O4

3D mesoporous rose-like nickel-iron selenide microspheres as advanced electrocatalysts for the oxygen evolution reaction

Jiahao Yu[1], Gongzhen Cheng[1], and Wei Luo[1,2] (✉)

[1] *College of Chemistry and Molecular Sciences, Wuhan University, Wuhan 430072, China*
[2] *Key Laboratory of Advanced Energy Materials Chemistry (Ministry of Education), Nankai University, Tianjin 300071, China*

Received: 16 July 2017
Revised: 23 August 2017
Accepted: 29 August 2017

KEYWORDS
transition metal selenide,
oxygen evolution reaction,
NiFeSe,
three-dimensional (3D),
rose-like microspheres

ABSTRACT

The development of efficient and stable non-noble metal-based electrocatalysts for the oxygen evolution reaction (OER) is one of the essential challenges for the upcoming hydrogen economy. Herein, three-dimensional (3D) mesoporous nickel iron selenide with rose-like microsphere architecture was directly grown on Ni foam via a successive two-step hydrothermal method. The unique 3D mesoporous rose-like morphology leads to a higher number of active sites as well as fast mass and electron transport through the entire electrode, and facilitates the release of O_2 bubbles formed during the OER catalysis. As a result, the synthesized $Ni_{0.76}Fe_{0.24}Se$ exhibits superior OER performances, with an ultralow overpotential of 197 mV needed to produce a current density of 10 mA·cm^{-2} in 1 M KOH, outperforming all transition metal selenide OER catalysts reported to date.

1 Introduction

Hydrogen is regarded as a promising energy carrier for future energy conversion and storage systems, due to its high energy density and environmental benignity [1–5]. Electrochemical and photoelectrochemical water splitting involving the cathodic hydrogen evolution reaction (HER) and anodic oxygen evolution reaction (OER) have been identified as the most eco-friendly and cost-effective approaches for hydrogen production [6–10]. However, the OER is affected by sluggish reaction kinetics, probably due to the multiproton-coupled electron transfer steps involved, and represents the bottleneck of the overall water splitting process [10–19]. Precious metal-based electrocatalysts such as IrO_2 and RuO_2 are considered state-of-the-art OER catalysts with lower overpotential (η) and improved efficiency, but the limited availability and corresponding high price of these metals severely limit their large-scale applications [20, 21]. Therefore, the development of non-noble metal OER catalysts with high activity and stability currently represents a crucial challenge.

Address correspondence to wluo@whu.edu.cn

Recently, transition metal-based electrocatalysts have emerged as a promising alternative to precious metal catalysts for the OER [22–28]. Among these materials, transition metal selenides (TMS) such as nickel selenide have attracted particular interest due to their low cost and high performances [9, 18, 28–30]. For instance, Alshareef and co-workers reported that $(Ni, Co)_{0.85}Se$ nanoarrays could achieve a current density of 10 $mA·cm^{-2}$ with an overpotential of 255 mV in the OER [28]. Sun et al. synthesized a Co-doped $NiSe_2$ nanoparticle film, capable of reaching 100 $mA·cm^{-2}$ with an overpotential of only 320 mV [31]. Li et al. fabricated an amorphous Fe-NiSe OER catalyst requiring an overpotential of only 233 mV to drive a current density of 10 $mA·cm^{-2}$, superior to that of NiSe [32]. Very recently, our group reported the colloidal synthesis of urchin-like Fe-doped $NiSe_2$ with an overpotential of 227 mV at a current density of 10 $mA·cm^{-2}$ in the OER [33]. Despite the significant efforts made in this direction, obtaining electrocatalysts with high efficiency and long-term stability still remains a significant challenge, due to the relatively low conductivity and limited surface area of these materials.

In general, the structure and morphology of the electrocatalyst can significantly affect its electrocatalytic activity [28, 34–39]. In the present work, we report a facile synthetic method for preparing three-dimensional (3D) porous Ni-FeSe microspheres with rose-like architecture on Ni foam via a successive two-step hydrothermal approach. Owing to the unique mesoporous architecture and to the strong electronic interaction between Ni, Fe, and Se, the resulting $Ni_{0.76}Fe_{0.24}Se$ exhibits exceptional OER catalytic performances. In particular, the present system requires an ultralow overpotential of only 197 mV to produce a current density of 10 $mA·cm^{-2}$, outperforming all transition metal selenide OER catalysts and most non-noble metal-based catalysts reported to date.

2 Experimental

2.1 Chemicals and materials

The materials employed in the experiments were used directly without any purification. Iron sulfate heptahydrate ($FeSO_4·7H_2O$, 99%–101%), nickel nitrate hexahydrate ($Ni(NO_3)_2·6H_2O$, 98%), ammonium fluoride (NH_4F, 96%), urea ($CO(NH_2)_2$, 99%), selenium powder (99%), sodium borohydride ($NaBH_4$, 98%), potassium hydroxide (KOH, 85.0%), and isopropyl alcohol (C_3H_8O, 99.7%) were obtained from Sinopharm Chemical Reagent Co., Ltd., whereas Nafion solution (5 wt.%) and Pt/C (Johnson Matthey Hispec 3600, 20 wt.%) were purchased from Shanghai Hesen Electric Co., Ltd. and Sigma-Aldrich Co., respectively.

2.2 Synthesis of $Ni_xFe_{1-x}Se$

Prior to utilization, Ni foam (NF, 2 cm × 3 cm) was carefully cleaned with ~ 37 wt.% concentrated HCl solution in an ultrasound bath for about 5 min to remove the NiO layer, and then acetone, ultrapure water, and absolute ethanol were used to thoroughly clean the Ni foam surface. In a typical procedure, $Ni(NO_3)_2·6H_2O$ (1 mmol), $FeSO_4·7H_2O$ (1 mmol), NH_4F (8 mmol), and urea (10 mmol) were dissolved in 36 mL of ultrapure water and stirred to form a transparent and homogeneous solution. The Ni foam and the aqueous solution were transferred to a 40 mL Teflon-lined stainless steel autoclave, which was sealed and maintained at 100 ℃ for 8 h in a drying oven. After washing thoroughly with distilled water and absolute ethanol, a NiFe-layered double hydroxide (LDH) grown on Ni foam was obtained. To prepare $Ni_{0.76}Fe_{0.24}Se$ nanoblossoms, Se powder (0.118 g) and $NaBH_4$ (0.13 g) were first added to 3 mL ultrapure water, followed by gentle stirring for 30 min and dropping 33 mL ethanol, to obtain an NaHSe solution. Then, the NiFe LDH was immersed into the freshly prepared NaHSe solution and transferred into the Teflon-lined stainless steel autoclave, which was heated at 180 ℃ for 12 h in an electric oven. After cooling down the autoclave, the sample was removed and washed with water and ethanol several times. The mass loading of the $Ni_{0.76}Fe_{0.24}Se$ catalyst layer was approximately 6.6 $mg·cm^{-2}$, determined by precise measurement. In addition, NiSe nanosheets, $Ni_{0.82}Fe_{0.18}Se$, and $Ni_{0.5}Fe_{0.5}Se$ microclusters with different $FeSO_4·7H_2O$: $Ni(NO_3)_2·6H_2O$ molar ratios (0, 1:3, 1:1, 3:1, for a total amount of 2 mmol) were fabricated following the same procedure described above. The actual Ni/Fe atomic ratios in the $Ni_xFe_{1-x}Se$ samples were determined by inductively

coupled plasma-atomic emission spectroscopy (ICP-AES) and are listed in Table S1 in the Electronic Supplementary Material (ESM).

2.3 Materials characterization

Powder X-ray diffraction (XRD) patterns were recorded on a Bruker D8-Advance X-ray diffractometer using a Cu Kα radiation source (λ = 0.154178 nm) with a scan rate of 6 °·min^{-1}. The morphologies of the samples were inspected by scanning electron microscopy (SEM, Zeiss Sigma), along with transmission electron microscopy (TEM) using a Tecnai G20 U-Twin microscope equipped with an energy dispersive X-ray (EDX) detector at an acceleration voltage of 200 kV. X-ray photoelectron spectroscopy (XPS) measurements were performed with a Thermo Fischer ESCALAB 250Xi spectrophotometer. N_2 adsorption/desorption isotherms were measured using a Quantachrome Quadrasorb Evo analyzer. ICP-AES measurements were performed on an IRIS Intrepid II XSP instrument.

2.4 Electrochemical measurements

Electrochemical measurements were performed with a CHI 760E electrochemical analyzer (CH Instruments, Chenhua Co., Shanghai, China). A conventional one-component three-electrode cell was used, including the present samples as the working electrode, an Hg/HgO electrode as the reference electrode in 1 M KOH filling solution, and platinum foil as the counter electrode. 1 M KOH was employed as the electrolyte solution. Before the test, the potential of the reference electrode was calibrated against the reversible hydrogen electrode (RHE), using a 20 wt.% Pt/C rotating disk electrode (RDE) at 1,600 rpm as the working electrode in a hydrogen saturated electrolyte; the RHE potential was estimated as the potential at which the current crossed zero. All potentials reported in the paper were *iR*-corrected according to the equation

$$E_{\mathrm{RHE}(iR\text{-corrected})} = E_{\mathrm{Hg/HgO}} + 0.915 - iR \quad (1)$$

where i is the current and R is the uncompensated ohmic electrolyte resistance (1 Ω) measured with a high-frequency alternating current (AC) impedance analyzer at 200 kHz under open-circuit potential (OCP) conditions. Two cycles of linear sweep voltammetry (LSV) were performed at 0.1 mV·s^{-1} between 0.3 and 0.9 V (vs. Hg/HgO), and the negative sweep curve was selected as the LSV curve. Tafel slopes were calculated based on the LSV curve by plotting the potential (vs. the RHE) against the logarithm of the current density. The electrochemical capacitance was determined using cyclic voltammetry (CV) measurements at different scan rates: 10, 20, 30, 40, and 50 mV·s^{-1}; the double-layer capacitance (C_{dl}) values were calculated from the slope of the current density vs. scan rate linear plot. The potential typically varied within a 0.1 V window centered at the OCP. Chronopotentiometry tests were carried out at a current density of 10 mA·cm^{-2}. The stability was evaluated by CV tests with a sweep rate of 100 mV·s^{-1} for 500 cycles. The overpotential (η) was calculated from the relation

$$\eta = E(\mathrm{RHE}) - 1.23\ \mathrm{V} \quad (2)$$

3 Results and discussion

A series of $Ni_xFe_{1-x}Se$ electrocatalysts were directly synthesized on Ni foam via a two-step hydrothermal process, as shown in Scheme 1 and discussed in the experimental section. The NiFe LDH precursor was prepared first; the distinctive peaks at 23.7°, 34.4°, 39.1°, 59.9°, and 61.3° in its powder XRD pattern (Fig. 1(a)) were attributed to the (002), (012), (200), (110), and (113) planes of α-$Ni(OH)_2$, in agreement with a previous report [40]. The other peaks at 44.5°, 51.8°,

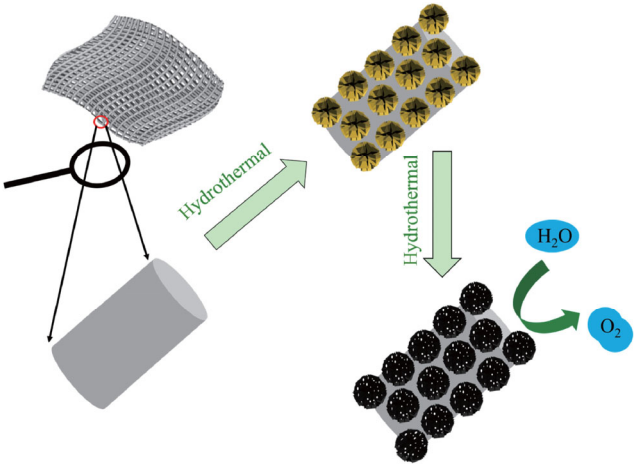

Scheme 1 Schematic illustration of the synthesis of 3D nanoporous $Ni_{0.76}Fe_{0.24}Se$ microspheres.

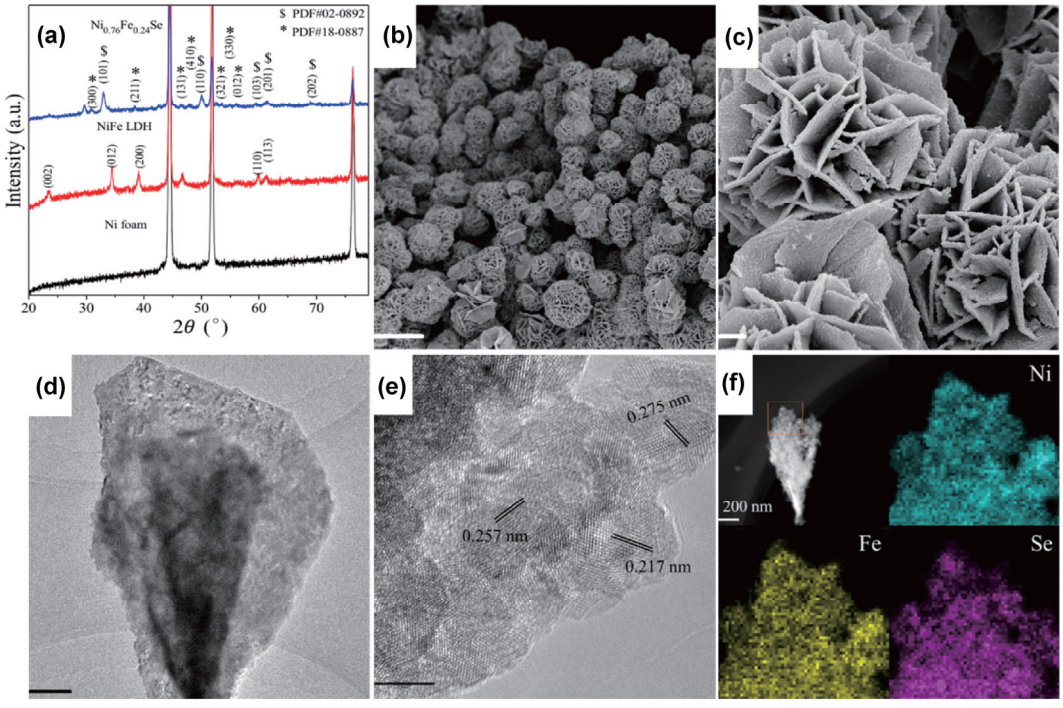

Figure 1 (a) XRD patterns of $Ni_{0.76}Fe_{0.24}Se$, NiFe LDH, and Ni foam. (b) and (c) SEM images of $Ni_{0.76}Fe_{0.24}Se$ microspheres. (d) TEM and (e) HRTEM images of $Ni_{0.76}Fe_{0.24}Se$ nanosheets. (f) STEM and EDX elemental mapping images. Scale bars: (b) 10 μm; (c) 500 nm; (d) 250 nm; (e) 5 nm; (f) 200 nm.

and 76.4° were assigned to the Ni foam. After selenization, new peaks at 30.8°, 38.5°, 46.4°, 47.9°, 53.5°, 55.0°, 56.0° were indexed to the (300), (211), (131), (410), (321), (330), and (012) reflections of makinenite NiSe (powder diffraction file (PDF) #18-0887), whereas peaks at 32.9°, 50.0°, 59.5°, 61.3°, and 68.9° were attributed to the (101), (110), (103), (201), and (202) planes of NiSe (PDF #02-0892). These data indicate the complete conversion of the NiFe LDH to NiFe selenide. The SEM images show that $Ni_{0.76}Fe_{0.24}Se$ maintains the rose-like microsphere architecture of the NiFe LDH during the selenization process, with diameter varying from 5 to 8 μm, as shown in Figs. 1(b), 1(c), and Fig. S1(a) in the ESM. The TEM images in Fig. 1(d) and Fig. S1(b) in the ESM indicate an increased roughness of the $Ni_{0.76}Fe_{0.24}Se$ nanosheets compared with the NiFe LDH precursor. The high-resolution TEM (HRTEM) image in Fig. 1(e) reveals well-resolved lattice fringes with spacings of 0.217, 0.257, and 0.275 nm, slightly larger than the 0.215, 0.256, and 0.274 nm spacings corresponding to the (211), (231), and (110) planes of NiSe, respectively, probably due to the consistent substitution of Fe for Ni [41]. The EDX spectrum (Fig. S2 in the ESM) confirms the co-existence of Ni, Fe, and Se. In addition, the scanning TEM (STEM) image and EDX elemental mapping images (Fig. 1(f)) further confirm the uniform distribution of Ni, Fe, and Se within the whole $Ni_{0.76}Fe_{0.24}Se$ nanosheets. N_2 adsorption–desorption measurements were performed to investigate the porous structure of $Ni_{0.76}Fe_{0.24}Se$. As shown in Fig. S3 in the ESM, the N_2 adsorption–desorption isotherm and the corresponding density functional theory (DFT) pore size distribution (inset) indicate the presence of mesopores with an average size of 5.2 nm in $Ni_{0.76}Fe_{0.24}Se$.

The N_2 adsorption–desorption isotherms of NiFe LDH and NiSe were also measured, and their Brunauer–Emmett–Teller (BET) surface areas were both calculated to be 14.3 $m^2 \cdot g^{-1}$ (Fig. S4 in the ESM).

We found that the added amount of Fe precursor is the key for the formation of the unique 3D rose-like architecture. As shown in Fig. S5 (in the ESM), the XRD patterns of different $Ni_xFe_{1-x}Se$ samples and NiSe are similar. The actual atomic ratios determined by ICP-AES are listed in Table S1 (in the ESM). As shown in Fig. S6 (in the ESM), a NiSe nanosheet array is

formed without Fe doping. However, despite the similar morphology to the $Ni_{0.76}Fe_{0.24}Se$ precursor, irregular aggregated nanoclusters of $Ni_{0.82}Fe_{0.18}Se$ and $Ni_{0.5}Fe_{0.5}Se$ are observed after selenization.

XPS measurements were performed to explore the surface structure of the $Ni_{0.76}Fe_{0.24}Se$ microspheres. The $3d_{3/2}$ and $3d_{5/2}$ peaks at 55.4 and 54.2 eV in Fig. 2(a) correspond to the Se 3d binding energies (BEs), whereas the peak at 58.9 eV is assigned to the oxidized metal selenide species. In the high-resolution Ni 2p spectrum (Fig. 2(b)), one spin-orbit doublet corresponding to Ni^{2+} and two shake-up satellites are observed, indicating the presence of NiSe. The other peak located at 852.5 eV is assigned to the exposed Ni foam. The Fe 2p spectrum (Fig. 2(c)) shows two main peaks at 711.0 and 723.5 eV, which match well with the typical $2p_{1/2}$ and $2p_{3/2}$ peaks of Fe^{3+}. Another peak located at 706.4 eV corresponds to Fe^{2+}. In addition, compared with NiSe, the Se 3d and Ni 2p peaks are shifted toward higher BEs, suggesting a strong electronic interaction between Se, Ni, and Fe in the $Ni_{0.76}Fe_{0.24}Se$ sample [3, 42].

The electrocatalytic OER activity in 1 M KOH of $Ni_xFe_{1-x}Se$ samples with different molar ratios, as well as that of NiSe, NiFe LDH, and Ni foam were evaluated using a standard three-electrode system and applying representative *iR*-corrected polarization curves with a sweeping rate of 0.1 $mV \cdot s^{-1}$. As shown in Fig. 3(a), $Ni_{0.76}Fe_{0.24}Se$ exhibits the highest intrinsic OER activity among all catalysts tested. In particular, it needs an overpotential of only 197 mV to reach a current density of 10 $mA \cdot cm^{-2}$, which is much lower than the corresponding overpotentials of NiSe (217 mV), NiFe LDH (220 mV), Ni foam (408 mV), $Ni_{0.82}Fe_{0.18}Se$ (205 mV), and $Ni_{0.5}Fe_{0.5}Se$ (205 mV). Besides, $Ni_{0.76}Fe_{0.24}Se$ could achieve large current densities of 200 and 400 $mA \cdot cm^{-2}$ at overpotentials of 294 and 353 mV, respectively. To the best of our knowledge, the catalytic activity of $Ni_{0.76}Fe_{0.24}Se$ is higher that of all TMS OER catalysts and of most non-noble metal electrocatalysts reported to date, as shown in Table S2 in the ESM. The superior OER performance of $Ni_{0.76}Fe_{0.24}Se$ was further investigated by the Tafel plots shown in Fig. 3(b). The Tafel slope of $Ni_{0.76}Fe_{0.24}Se$ is calculated to be 56 $mV \cdot dec^{-1}$, close to those of $Ni_{0.82}Fe_{0.18}Se$ (62 $mV \cdot dec^{-1}$) and $Ni_{0.5}Fe_{0.5}Se$ (60 $mV \cdot dec^{-1}$), and much smaller than those of NiSe (73 $mV \cdot dec^{-1}$) and Ni foam (139 $mV \cdot dec^{-1}$), suggesting a more favorable OER reaction kinetics in $Ni_xFe_{1-x}Se$ [43, 44].

The stability of the catalyst under different operating conditions is an important criterion for evaluating the practical applicability of an efficient OER catalyst. As shown in Fig. 3(c), the $Ni_{0.76}Fe_{0.24}Se$ electrocatalyst maintained a current density of 10 $mA \cdot cm^{-2}$ over a period of 60,000 s during the OER process. Moreover,

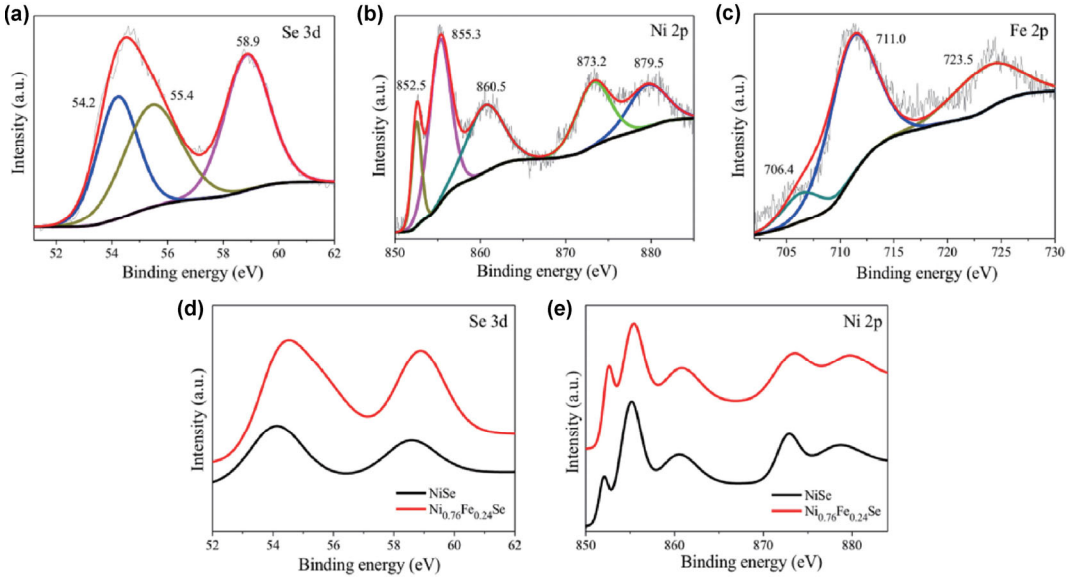

Figure 2 XPS spectra in the (a) Se 3d, (b) Ni 2p, (c) Fe 2p regions of $Ni_{0.76}Fe_{0.24}Se$ and in the (d) S 2p, (e) Ni 2p regions of $Ni_{0.76}Fe_{0.24}Se$ and NiSe.

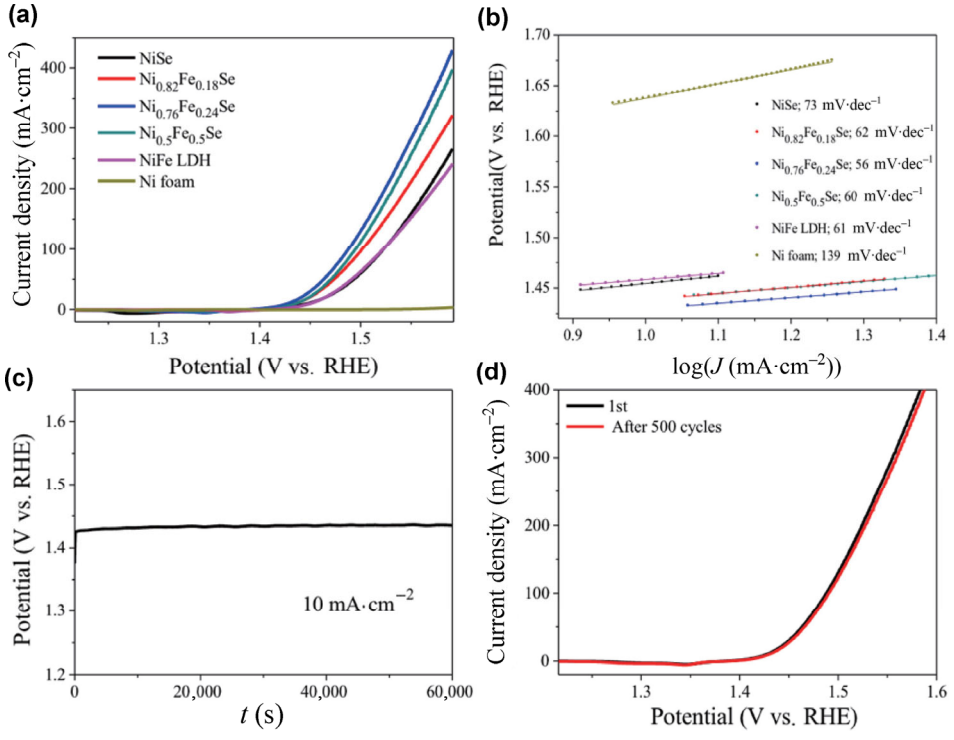

Figure 3 (a) *iR*-corrected LSV curves for the OER of $Ni_xFe_{1-x}Se$, NiFe LDH, NiSe, and Ni foam, measured at a scan rate of 0.1 mV·s^{-1}. (b) Tafel plots of $Ni_xFe_{1-x}Se$, NiFe LDH, NiSe, and Ni foam. (c) Chronopotentiometric measurements for the OER at 10 mA·cm^{-2} (without *iR* correction). (d) Durability tests (500 cycles, *iR*-corrected) using $Ni_{0.76}Fe_{0.24}Se$ as catalyst.

Fig. 3(d) shows that after long-term cycling (500 cycles), $Ni_{0.76}Fe_{0.24}Se$ exhibited almost the same polarization curve (red curve) as before (black curve). These results imply that $Ni_{0.76}Fe_{0.24}Se$ possesses superior operating stability in long-term electrochemical OER processes. Moreover, no obvious morphology changes were observed in the SEM images after the stability test (Figs. S7 and S8(a) in the ESM). As shown in Fig. S9 in the ESM, the XRD pattern of $Ni_{0.76}Fe_{0.24}Se$ after the OER stability test still exhibits peaks at 32.9° and 50.0° corresponding to the (101) and (110) planes of NiSe, respectively. The XPS spectra of $Ni_{0.76}Fe_{0.24}Se$ after the OER stability test, shown in Fig. S10 (in the ESM), highlight a decreased intensity of the Se 3d peak, with the formation of Ni (Fe) oxo/hydroxide (852.8 eV). At the same time, two spin-orbit doublets attributed to Fe^{3+} and Ni^{2+}, along with their shake-up satellites, are observed in the Fe 2p and Ni 2p regions, respectively. In addition, as shown in Fig. S8(b) (in the ESM), no obvious lattice fringes are observed, consistent with the XRD results, indicating the amorphous nature of the *in situ*-formed Ni (Fe) oxo/hydroxide [16].

These results suggest that amorphous Ni-Fe oxo/hydroxide species are formed on the surface of the catalyst, and might act as efficient active sites during the OER process, consistent with previous reports [16, 17, 45, 46]. Moreover, electrochemical impedance spectroscopy (EIS) measurements were conducted to gain further insight into the electron-transfer kinetics during the OER catalysis, as shown in Fig. S11 (in the ESM). The first semicircle in the high-frequency region represents the charge transfer resistance (R_s) from the solution to the electrode surface, while the semicircle in the low-frequency region is related to the charge-transfer resistance (R_{ct}) inside the electrode [47]. $Ni_{0.76}Fe_{0.24}Se$ exhibits a much smaller Nyquist semicircle diameter than NiFe LDH and NiSe, highlighting its lowest R_{ct}, which results in a much faster electron transfer during the OER process. To evaluate the electrochemically active surface area (ECSA) of the electrocatalysts, cyclic voltammetry measurements were performed at different scan rates (from 10 to 50 mV·s^{-1}) to measure the double-layer capacitance. As displayed in Fig. 4, the C_{dl} of $Ni_{0.76}Fe_{0.24}Se$ is measured to be

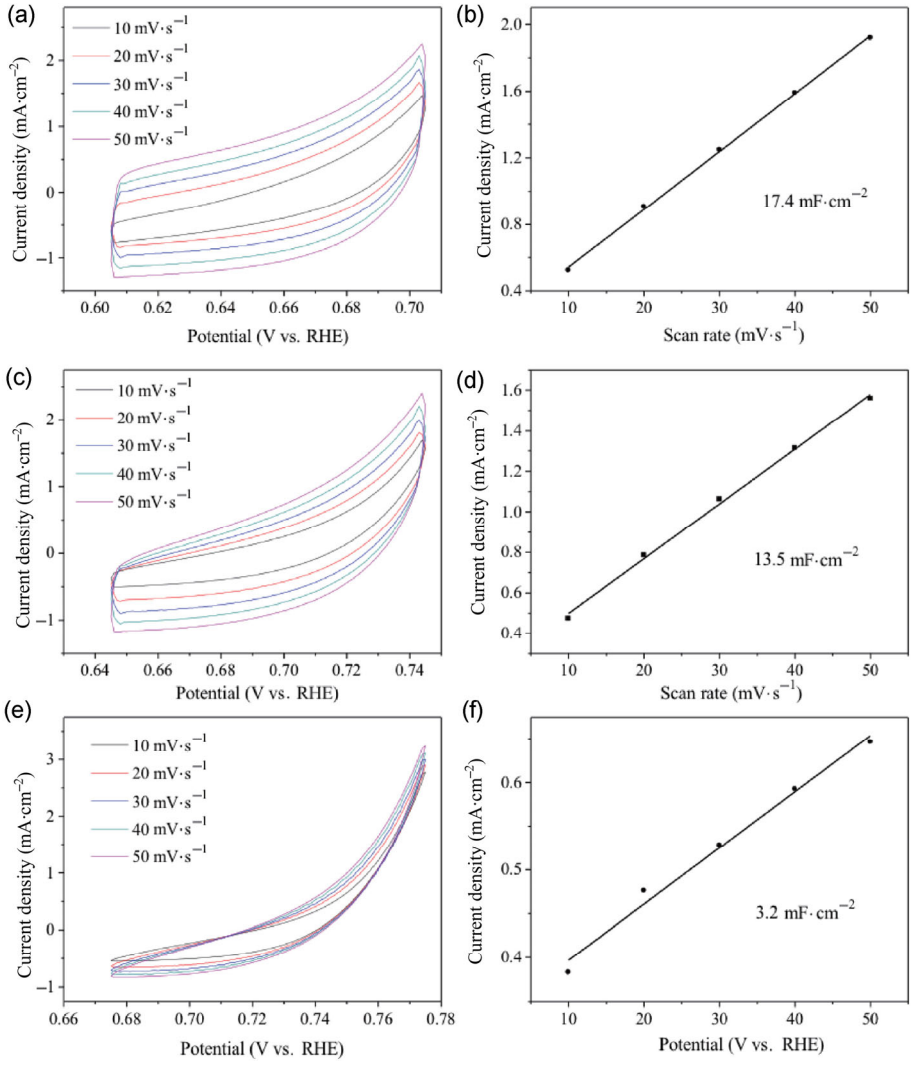

Figure 4 Cyclic voltammetry curves of (a) $Ni_{0.76}Fe_{0.24}Se$, (c) NiSe, and (e) NiFe LDH tested at various scan rates, ranging from 10 to 50 mV·s^{-1}. Scan rate dependence of the current densities of (b) $Ni_{0.76}Fe_{0.24}Se$, (d) NiSe, and (f) NiFe LDH (vs. RHE).

17.4 mF·cm^{-2}, higher than those of NiSe (13.5 mF·cm^{-2}) and NiFe LDH (3.2 mF·cm^{-2}), suggesting the presence of relatively larger active areas in $Ni_{0.76}Fe_{0.24}Se$.

The enhanced OER performance of $Ni_{0.76}Fe_{0.24}Se$ might be attributed to its unique 3D rose-like architecture and ternary composition. In particular, the highly open rose-like hierarchical architecture could greatly increase the exposure of the active sites, and further increase the contact with electrolyte. Moreover, the mesoporous structure provides accessible channels for mass/electron transport, and facilitates the release of O_2 bubbles formed during the OER catalysis. In addition, the optimal doping of Fe source alters not only the morphology but also the electronic structure of NiSe, resulting in strong electronic interactions between Ni, Fe, and Se, which further enhance the trapping of OH^- species. Moreover, Ni foam, as an efficient substrate, could improve the conductivity and make active materials widely distributed, enhancing mass/electron transport.

4 Conclusions

In summary, 3D mesoporous nickel iron selenides with rose-like microsphere morphology have been directly grown on Ni foam via a successive two-step hydrothermal method. The unique 3D porous rose-like architecture of $Ni_{0.76}Fe_{0.24}Se$ considerably increases the

number of active sites, provides accessible channels for mass/electron transport, and facilitates the release of O_2 bubbles formed during the OER catalysis. Thanks to this unique morphology and to the strong electronic interaction between Ni, Fe, and Se, the as-prepared $Ni_{0.76}Fe_{0.24}Se$ exhibits excellent OER catalytic activity with ultralow overpotential and Tafel slope, as well as superior stability in alkaline solutions. The outstanding catalytic performance and low cost of $Ni_{0.76}Fe_{0.24}Se$ make it a promising candidate for OER catalysis in renewable energy systems. The simple synthetic route presented here could also inspire the development of other transition metal selenide, sulphide, and phosphide materials for further applications.

Acknowledgements

This work was financially supported by the National Natural Science Foundation of China (Nos. 21571145 and 21633008), the Fundamental Research Funds for the Central Universities and Large-scale Instrument and Equipment Sharing Foundation of Wuhan University.

Electronic Supplementary Material: Supplementary material (SEM images, EDX spectrum, N_2 adsorption–desorption isotherm and pore size distribution, XRD patterns, XPS spectra, EIS spectra) is available in the online version of this article at https://doi.org/10.1007/s12274-017-1832-8.

References

[1] Chu, S.; Majumdar, A. Opportunities and challenges for asustainable energy future. *Nature* **2012**, *488*, 294–303.

[2] Zou, X. X.; Zhang, Y. Noble metal-free hydrogen evolution catalysts for water splitting. *Chem. Soc. Rev.* **2015**, *44*, 5148–5180.

[3] Liu, T. T.; Liu, D. N.; Qu, F. L.; Wang, D. X.; Zhang, L.; Ge, R. X.; Hao, S.; Ma, Y. J.; Du, G.; Asiri, A. M. et al. Enhanced electrocatalysis for energy-efficient hydrogen production over CoP catalyst with nonelectroactive Zn as a promoter. *Adv. Energy Mater*. **2017**, *7*, 1700020.

[4] Yang, F. L.; Chen, Y. T.; Cheng, G, Z.; Chen, S. L.; Luo, W. Ultrathin nitrogen-doped carbon coated with CoP for efficient hydrogen evolution. *ACS Catal.* 2017, *7*, 3824–3831.

[5] Long, X.; Li, G. X.; Wang, Z. L.; Zhu, H. Y.; Zhang, T.; Xiao. S.; Guo, W. Y.; Yang, S. H. Metallic iron–nickel sulfide ultrathin nanosheets as a highly active electrocatalyst for hydrogen evolution reaction in acidic media.*J. Am. Chem. Soc.* **2015**, *137*, 11900–11903.

[6] Liu, J.; Liu, Y.; Liu, N. Y.; Han, Y. Z.; Zhang, X.; Huang, H.; Lifshitz, Y.; Lee, S. T.; Zhong, J.; Kang, Z. H. Metal-free efficient photocatalyst for stable visible water splitting via a two-electron pathway. *Science* **2015**, *347*, 970–974.

[7] Du, C.; Yang, L.; Yang, F. L.; Cheng, G. Z.; Luo, W. Nest-like NiCoP for highly efficient overall water splitting. *ACS Catal.* **2017**, *7*, 4131–4137.

[8] Wu, Y. Y.; Liu, Y. P.; Li, G. D.; Zou, X.; Lian, X. R.; Wang, D. J.; Sun, L.; Asefa, T.; Zou, X. X. Efficient electrocatalysis of overall water splitting by ultrasmall $Ni_xCo_{3-x}S_4$ coupled Ni_3S_2 nanosheet arrays. *Nano Energy* **2017**, *35*,161–170.

[9] Sun, C. C.; Dong, Q. C.; Yang, J.; Dai, Z. Y.; Lin, J. J.; Chen, P.; Huang, W.; Dong, X. C.Metal–organic framework derived $CoSe_2$ nanoparticles anchored on carbon fibers as bifunctional electrocatalysts for efficient overall water splitting. *Nano Res*. **2016**, *9*, 2234–2243.

[10] Wang, J.; Zhong, H. X.; Wang, Z. L.; Meng, F. L.; Zhang, X. B. Integrated three-dimensional carbon paper/carbon tubes/cobalts-sulfide sheets as an efficient electrode for overall water splitting. *ACS Nano* **2016**, *10*, 2342–2348.

[11] Chen, P. Z.; Xu, K.; Fang, Z. W.; Tong, Y.; Wu, J. C.; Lu, X. L.; Peng, X.; Ding, H.; Wu, C. Z.; Xie, Y. Metallic Co_4N porous nanowire arrays activated by surface oxidation as electrocatalysts for the oxygen evolution reaction. *Angew. Chem., Int. Ed*. **2015**, *54*, 14710–14714.

[12] Zhang, W.; Wu, Y. Z.; Qi, J.; Chen, M. X.; Cao, R. A thin NiFe hydroxide film formed by stepwise electrodeposition strategy with significantly improved catalytic water oxidation efficiency. *Adv. Energy Mater*. **2017**, *7*, 1602547.

[13] Wan, S. H.; Qi, J.; Zhang, W.; Wang, W. N.; Zhang, S. K.; Liu, K. Q.; Zheng, H. Q.; Sun, J. L.; Wang, S. Y.; Cao, R. Hierarchical Co(OH)F superstructure built by low-dimensional substructures for electrocatalytic water oxidation. *Adv. Mater*. **2017**, *29*, 1700286.

[14] Chen, M. X.; Wu, Y. Z.; Han, Y. Z.; Lin, X. H.; Sun, J. L.; Zhang, W.; Cao, R. An iron-based film for highly efficient electrocatalytic oxygen evolution from neutral aqueous solution. *ACS Appl. Mater. Interfaces* **2015**, *7*, 21852–21859.

[15] Guo, D. Y.; Qi, J.; Zhang, W.; Cao, R. Surface electrochemical modification of a nickel substrate to prepare a NiFe-based electrode for water oxidation. *ChemSusChem* **2017**, *10*, 394–400.

[16] Stern, L. A.; Feng, L. G.; Song, F.; Hu, X. L. Ni_2P as a Janus catalyst for water splitting: The oxygen evolution activity of Ni_2P nanoparticles. *Energy Environ. Sci.* **2015**, *8*, 2347–2351.

[17] Xu, X.; Song, F.; Hu, X. L. A nickel iron diselenide-derived efficient oxygen-evolution catalyst. *Nat. Commun.* **2016**, *7*, 12324.

[18] Zhao, X.; Zhang, H. T.; Yan. Y.; Cao, J. H.; Li, X. Q.; Zhou, S. M.; Peng, Z. M.; Zeng, J. Engineering the electrical conductivity of lamellar silver-doped cobalt(II) selenide nanobelts for enhanced oxygen evolution. *Angew. Chem., Int. Ed.* **2017**, *56*,328–332.

[19] Gong, M.; Dai, H. J. A mini review of NiFe-based materials as highly active oxygen evolution reaction electrocatalysts. *Nano Res.* **2015**, *8*, 23–39.

[20] Lee, Y.; Suntivich, J.; May, K. J.; Perry, E. E.; Shao-Horn, Y. Synthesis and activities of rutile IrO_2 and RuO_2 nanoparticles for oxygen evolution in acid and alkaline solutions. *J. Phys. Chem. Lett.* **2012**, *3*, 399–404.

[21] Wang, J.; Zhong, H. X.; Qin, Y. L.; Zhang, X. B. An efficient three-dimensional oxygen evolution electrode. *Angew. Chem., Int. Ed.* **2013**, *52*, 5248–5253.

[22] Fan, X. J.; Peng, Z. W.; Ye, R. Q.; Zhou, H. Q.; Guo, X. M_3C (M: Fe, Co, Ni) nanocrystals encased in graphene nanoribbons: An active and stable bifunctional electrocatalyst for oxygen reduction and hydrogen evolution reactions. *ACS Nano* **2015**, *9*, 7407–7418.

[23] McCrory, C. C. L.; Jung, S.; Peters, J. C.; Jaramillo, T. F. Benchmarking heterogeneous electrocatalysts for the oxygen evolution reaction. *J. Am. Chem. Soc.* **2013**, *135*, 16977–16987.

[24] Masa, J.; Weide, P.; Peeters, D.; Sinev, I.; Xia, W.; Sun, Z. Y.; Somsen, C.; Muhler, M.; Schuhmann, W. Amorphous cobalt boride (Co_2B) as a highly efficient nonprecious catalyst for electrochemical water splitting: Oxygen and hydrogen evolution. *Adv. Energy Mater.* **2016**, *6*, 1502313.

[25] Yan, K.; Wu, G. S.; Jin, W. Recent advances in the synthesis of layered, double-hydroxide-based materials and their applications in hydrogen and oxygen evolution. *Energy Technol.* **2016**, *4*, 354–368.

[26] Bai, Y. J.; Fang, L.; Xu, H. T.; Gu, X.; Zhang, H. J.; Wang, Y. Strengthened synergistic effect of metallic M_xP_y (M = Co, Ni, and Cu) and carbon layer via peapod-like architecture for both hydrogen and oxygen evolution reactions. *Small* **2017**, *13,* 1603718.

[27] Yan, Y.; Xia, B. Y.; Li, N.; Xu, Z. C.; Fisher, A.; Wang, X. Vertically oriented MoS_2 and WS_2 nanosheets directly grown on carbon cloth as efficient and stable 3-dimensional hydrogen-evolving cathodes. *J. Mater. Chem. A***2015**, *3*, 131–135.

[28] Xia, C.; Jiang, Q.; Zhao, C.; Hedhili, M. N.; Alshareef, H. N. Selenide-based electrocatalysts and scaffolds for water oxidation applications. *Adv. Mater.* **2016**, *28*, 77–85.

[29] Liu, X. B.; Liu, Y. C.; Fan, L. Z. MOF-derived $CoSe_2$ microspheres with hollow interiors as high-performance electrocatalysts for enhanced oxygen evolution reaction. *J. Mater. Chem. A* **2017**, *5*, 15310–15314.

[30] Sivanantham, A.; Shanmugam, S. Nickel selenide supported on nickel foam as an efficient and durable non-precious electrocatalyst for the alkaline water electrolysis. *Appl. Catal. B: Environ.* **2017**, *203*, 485–493.

[31] Liu, T. T.; Asiri, A. M.; Sun, X. P. Electrodeposited Co-doped $NiSe_2$ nanoparticles film: A good electrocatalyst for efficient water splitting. *Nanoscale* **2016**, *8*, 3911–3915.

[32] Zhao, Q.; Zhong, D. Z.; Liu, L.; Li, D. D.; Hao, G. Y.; Li, J. P. Facile fabrication of robust 3D Fe-NiSe nanowires supported on nickel foam as a highly efficient, durable oxygen evolution catalyst. *J. Mater. Chem. A* **2017**, *5*, 14639–14645.

[33] Du, Y. S.; Cheng, G. Z.; Luo, W. Colloidal synthesis of urchin-like Fe doped $NiSe_2$ for efficient oxygen evolution. *Nanoscale* **2017**, *9*, 6821–6825.

[34] Xie, J. F.; Zhang, H.; Li, S.; Wang, R. X.; Sun, X.; Zhou, M.; Zhou, J. F.; Lou, X. W.; Xie, Y. Defect-rich MoS_2 ultrathin nanosheets with additional active edge sites for enhanced electrocatalytic hydrogen evolution. *Adv. Mater.* **2013**, *25*, 5807–5813.

[35] You, B.; Jiang, N.; Sheng, M. L.; Bhushan, M. W.; Sun, Y. J. Hierarchically porous urchin-like Ni_2P superstructures supported on nickel foam as efficient bifunctional electrocatalysts for overall water splitting. *ACS Catal.* **2016**, *6*, 714–721.

[36] Wang, D. Y.; Gong, M.; Chou, H. L.; Pan, C. J.; Chen, H. A.; Wu, Y. P.; Lin, M. C.; Guan, M. Y.; Yang, J.; Chen, C. W. et al. Highly active and stable hybrid catalyst of cobalt-doped FeS_2 nanosheets–carbon nanotubes for hydrogen evolution reaction. *J. Am. Chem. Soc.* **2015**, *137*, 1587–1592.

[37] Tian, J. Q.; Liu, Q.; Cheng, N. Y.; Asiri, A. M.; Sun, X. P. Self-supported Cu_3P nanowire arrays as an integrated high-performance three-dimensional cathode for generating hydrogen from water. *Angew. Chem., Int. Ed.* **2014**, *53*, 9577–9581.

[38] Wang, Z. Q.; Zeng, S.; Liu, W. H.; Wang, X. W.; Li, Q. W.; Zhao, Z. G.; Geng, F. X. Coupling molecularly ultrathin sheets of NiFe-layered double hydroxide on $NiCo_2O_4$ nanowire arrays for highly efficient overall water-splitting activity. *ACS Appl. Mater. Interfaces* **2017**, *9*, 1488–1495.

[39] Liu, J.; Wang, J. S.; Zhang, B.; Ruan, Y. J.; Lv, L.; Ji, X.; Xu, K.; Miao, L.; Jiang, J. J. Hierarchical $NiCo_2S_4$@NiFe LDH heterostructures supported on nickel foam for enhanced overall-water-splitting activity. *ACS Appl. Mater. Interfaces* **2017**, *9*, 15364–15372.

[40] Lu, Z. Y.; Xu, W. W.; Zhu, W.; Yang, Q.; Lei, X. D.; Liu,

J. F.; Li, Y. P.; Sun, X. M.; Duan, X. Three-dimensional NiFe layered double hydroxide film for high-efficiency oxygen evolution reaction. *Chem. Commun.* **2014**, *50*, 6479–6482.

[41] Tang, C.; Gan, L. F.; Zhang, R.; Lu, W. B.; Jiang, X. E.; Asiri, A. M.; Sun, X. P.; Wang, J.; Chen, L. Ternary $Fe_{1-x}Co_xP$ nanowire array as a robust hydrogen evolution reaction electrocatalyst with Pt-like activity: Experimental and theoretical insight. *Nano Lett.* **2016**, *16*, 6617–6621.

[42] Yu, J.; Li, Q. Q.; Li, Y.; Xu, C. Y.; Zhen, L.; Dravid, V. P.; Wu, J. S. Ternary metal phosphide with triple-layered structure as a low-cost and efficient electrocatalyst for bifunctional water splitting. *Adv. Funct. Mater.* **2016**, *26*, 7644–7651.

[43] Song, J. H.; Zhu, C. Z.; Xu, B. Z.; Fu, S. F.; Engelhard, M. H.; Ye, R. F.; Du, D.; Beckman, S. P.; Lin, Y. H. Bimetallic cobalt-based phosphide zeoliticimidazolate framework: CoP_x phase-dependent electrical conductivity and hydrogen atom adsorption energy for efficient overall water splitting. *Adv. Energy Mater.* **2017**, *7*, 1601555.

[44] Chen, G. F.; Ma, T. Y.; Liu, Z. Q.; Li, N.; Su, Y. Z.; Davey, K.; Qiao, S. Z. Efficient and stable bifunctional electrocatalysts Ni/Ni_xM_y(M = P, S) for overall water splitting. *Adv. Funct. Mater.* **2016**, *26*, 3314–3323.

[45] Chen, W.; Liu, Y. Y.; Li, Y.; Sun, J.; Qiu, Y. C.; Liu, C.; Zhou, G. M.; Cui, Y. *In situ* electrochemically derived nanoporous oxides from transition metal dichalcogenides for active oxygen evolution catalysts. *Nano Lett.* **2016**, *16*, 7588–7596.

[46] Panda, C.; Menezes, P. W.; Walter, C.; Yao, S. L.; Miehlich, M. E.; Gutkin, V.; Meyer, K.; Driess, M. From a molecular 2Fe-2Se precursor to a highly efficient iron diselenide electrocatalyst for overall water splitting. *Angew. Chem., Int. Ed.* **2017**, *56*, 10506–10510.

[47] Zhang, W.; Qi, J.; Liu, K. Q.; Cao, R. A nickel-based integrated electrode from an autologous growth strategy for highly efficient water oxidation. *Adv. Energy Mater.* **2016**, *6*, 1502489.